RESEARCH ARTICLE

Deep learning-guided attenuation correction in the image domain for myocardial perfusion SPECT imaging

Samaneh Mostafapour[1,†], Faeze Gholamiankhah[2,†], Sirwan Maroufpour[3], Mehdi Momennezhad[4], Mohsen Asadinezhad[1], Seyed Rasoul Zakavi[4], Hossein Arabi[5] and Habib Zaidi [5,6,7,8,*]

[1]Department of Radiology Technology, Faculty of Paramedical Sciences, Mashhad University of Medical Sciences, Mashhad, Iran; [2]Department of Medical Physics, Faculty of Medicine, Shahid Sadoughi University of Medical Sciences, Yazd, Iran; [3]Department of Medical Physics, Faculty of Medicine, Mashhad University of Medical Sciences, Mashhad, Iran; [4]Nuclear Medicine Research Center, Mashhad University of Medical Sciences, Mashhad, Iran; [5]Division of Nuclear Medicine and Molecular Imaging, Geneva University Hospital, CH-1211 Geneva 4, Switzerland; [6]Geneva University Neurocenter, Geneva University, Geneva, Switzerland; [7]Department of Nuclear Medicine and Molecular Imaging, University of Groningen, University Medical Center Groningen, Groningen, the Netherlands and [8]Department of Nuclear Medicine, University of Southern Denmark, Odense, Denmark

*Corresponding author. E-mail: habib.zaidi@hcuge.ch https://orcid.org/0000-0001-7559-5297
†Equal contribution.

Abstract

We investigate the accuracy of direct attenuation correction (AC) in the image domain for myocardial perfusion SPECT (single-photon emission computed tomography) imaging (MPI-SPECT) using residual (ResNet) and UNet deep convolutional neural networks. MPI-SPECT ^{99m}Tc-sestamibi images of 99 patients were retrospectively included. UNet and ResNet networks were trained using non-attenuation-corrected SPECT images as input, whereas CT-based attenuation-corrected (CT-AC) SPECT images served as reference. Chang's calculated AC approach considering a uniform attenuation coefficient within the body contour was also implemented. Clinical and quantitative evaluations of the proposed methods were performed considering SPECT CT-AC images of 19 subjects (external validation set) as reference. Image-derived metrics, including the voxel-wise mean error (ME), mean absolute error, relative error, structural similarity index (SSI), and peak signal-to-noise ratio, as well as clinical relevant indices, such as total perfusion deficit (TPD), were utilized. Overall, AC SPECT images generated using the deep learning networks exhibited good agreement with SPECT CT-AC images, substantially outperforming Chang's method. The ResNet and UNet models resulted in an ME of -6.99 ± 16.72 and -4.41 ± 11.8 and an SSI of 0.99 ± 0.04 and 0.98 ± 0.05, respectively. Chang's approach led to ME and SSI of 25.52 ± 33.98 and 0.93 ± 0.09, respectively. Similarly, the clinical evaluation revealed a mean TPD of $12.78 \pm 9.22\%$ and $12.57 \pm 8.93\%$ for

ResNet and UNet models, respectively, compared to 12.84 ± 8.63% obtained from SPECT CT-AC images. Conversely, Chang's approach led to a mean TPD of 16.68 ± 11.24%. The deep learning AC methods have the potential to achieve reliable AC in MPI-SPECT imaging.

1. Introduction

Single-photon emission computed tomography (SPECT) myocardial perfusion imaging (MPI) is a widely used imaging modality in the clinical diagnosis of various cardiovascular diseases. This non-invasive examination technique plays a critical role in the evaluation of myocardial ischemia, coronary artery disease, and risk classification. SPECT imaging reveals cardiac physiology that would lead to earlier detection of pathophysiology or cardiac damage before the occurrence of morphological damage, wherein the former could likely be reversed (particularly in the early stages; Hachamovitch *et al.*, 1998; Iskander & Iskandrian, 1998; Russell & Zaret, 2006).

The quality of SPECT-MPI images is fundamental in the relevance of the outcomes of this diagnostic procedure, having a direct impact on the diagnostic or prognostic accuracy. A number of physical degrading factors limit the quality and the quantitative accuracy of reconstructed images in nuclear medical imaging in general and SPECT imaging in particular. These include photon attenuation, Compton scattering, septal penetration, and partial volume effect resulting from the limited spatial resolution of SPECT cameras. Various strategies were devised to compensate for the above-mentioned degrading factors aiming at improving the overall diagnostic accuracy and efficacy of SPECT imaging (Garcia, 2007; Arabi & Asl, 2010; Cuocolo, 2011; Sajedi *et al.*, 2014; Zeraatkar *et al.*, 2014).

Attenuated and scattered photons within the body would affect prominently the accuracy and specificity of SPECT-MPI since they vary noticeably (in terms of distribution and intensity) from one patient to another. They also reduce the accuracy of SPECT quantification and the physicians' confidence for the interpretation of images owing to the appearance of pseudo-perfusion or metabolic defects. This originates from the attenuation of photons within the human body, which varies significantly in inhomogeneously attenuation regions, such as the thorax, causing an apparent decrease in the tracer uptake. The diaphragm in men, breast in women, lateral chest walls, and abdomen in patients with large body mass index are the most common sources of photon attenuation artefacts in MPI SPECT imaging (Garcia, 2007; Fukushima & Kumita, 2016; Raza *et al.*, 2016).

Various strategies were developed/employed to diminish the adverse impact of photon attenuation in SPECT-MPI. This includes prone imaging (Singh *et al.*, 2007; Genovesi *et al.*, 2011), electrocardiography (ECG)-gated SPECT imaging (Genovesi *et al.*, 2011), and incorporation of attenuation compensation within iterative image reconstruction algorithms (Mostafapour *et al.*, 2021a). Prone imaging helps to address diaphragmatic attenuation, but it is challenged by the need for longer acquisition time, loss of image contrast, and inefficiency in dealing with breast attenuation (Garcia, 2007; Singh *et al.*, 2007). Attenuation correction (AC) in SPECT-MPI improves diagnostic accuracy and normalcy rate, which enables the interpretation of images with confidence, thus eliminating the need for a rest study in normal patients (Esteves *et al.*, 2005; Masood *et al.*, 2005; Garcia, 2007).

AC in SPECT imaging is commonly performed using one of two generic approaches: transmissionless and transmission-based methods. In transmission-based methods, regarded as the standard/reference AC approach, an external radionuclide-based transmission scan or CT scan is used to generate a patient-specific attenuation map (Zaidi & Hasegawa, 2003). Since the advent of the hybrid SPECT and CT scanners, combining emission and transmission imaging modalities into a single system, CT-based AC has become the commonly used standard AC approach in SPECT imaging. Besides providing high-resolution structural images (complementary anatomical information), the technique is able to generate patient-specific AC maps with relatively low noise and high image quality (Raza *et al.*, 2016). However, CT-based AC maps commonly suffer from misalignment errors between emission and transmission scans owing to bulk motion or involuntary patient movement in addition to increasing patients' radiation dose (Goetze *et al.*, 2007; Saleki *et al.*, 2019; Shi *et al.*, 2020).

Transmissionless approaches generate attenuation maps through defining body contour and assuming a uniform distribution of attenuation coefficients within the body. AC factors could also be estimated from the measured emission data. These approaches suffer from a lack of patient specificity (ignoring the inhomogeneity of tissues within the body) or high noise levels (Shi *et al.*, 2020; Mostafapour *et al.*, 2021a). When structural magnetic resonance (MR) images are available, synthetic CT images could be estimated from the MR images to perform AC (Marshall *et al.*, 2011).

The same challenge is faced in positron emission tomography (PET), wherein several attempts have been made to cope with this issue in the absence of conventional transmission or CT scans (Mehranian *et al.*, 2016; Arabi *et al.*, 2018). These methods, mostly developed for hybrid PET/MRI scanners, rely on concurrent structural MR images to generate synthetic CT images for PET attenuation and scatter correction. These include the segmentation-based (Arabi *et al.*, 2015; Arabi & Zaidi, 2020c), atlas-based (Arabi & Zaidi, 2016, 2017), and joint attenuation and emission reconstruction (Mehranian & Zaidi, 2015; Mehranian *et al.*, 2016). Recently, artificial intelligence-based approaches, in particular deep learning algorithms, have revolutionized the generation of synthetic CT images (Tankyevych *et al.*, 2021). Deep learning approaches enable the direct generation of accurate synthetic CT images from MR images (Arabi *et al.*, 2019; Bahrami *et al.*, 2020), estimation of patient-specific AC maps from the emission data (Arabi *et al.*, 2020), and application of direct attenuation and scatter correction in the image domain without the need for anatomical images (Arabi *et al.*, 2020; Mostafapour *et al.*, 2021b).

In this work, we set out to investigate the accuracy of direct attenuation and scatter correction in the image domain for SPECT-MPI using the residual and UNet deep neural networks. Considering our previous experience with different network architectures, ResNet and UNet exhibited superior performance for regression problems (Arabi & Zaidi, 2020b; Shiri *et al.*, 2020; Bahrami *et al.*, 2021; Gholamiankhah *et al.*, 2021). Hence, they were selected in this study. We also examined GAN-based models for our regression problem, wherein the ResNet and UNet models exhibited relatively better performance (Bahrami *et al.*, 2021; Gholamiankhah *et al.*, 2021). Nevertheless, there would be

Table 1: Number of normal subjects, normal subjects with image artefacts, and patients with cardiac defects. The total number of subjects is 99.

Normal	Normal (diaphragmatic attenuation artefact)	Normal (breast attenuation artefact)	Ischemia	Myocardial infarction (MI)	Ischemia and MI	Hypertrophic cardiomyopathy (HOCM)
74	5	2	7	4	5	2

other deep learning architectures that might exhibit similar or superior performance. A comprehensive comparative analysis is beyond the scope of this study but is definitely required to demonstrate the superiority of certain networks for a specific task (Yuan *et al.*, 2020; Chen *et al.*, 2021; Li *et al.*, 2021). These deep learning models were trained to directly estimate attenuation and scatter-corrected SPECT images from uncorrected images without the use of anatomical images. We also implemented Chang's calculated AC technique as a baseline for comparison of the different AC approaches in MPI-SPECT imaging. Chang's method, used on standalone SPECT cameras, assumes a uniform attenuation coefficient within the body contour (Chang, 1978; Takavar *et al.*, 2003; Akamatsu *et al.*, 2014). CT-based AC was considered as the standard/reference for qualitative and quantitative assessment of the deep learning-based AC approaches.

2. Materials and Methods

2.1 SPECT/CT data acquisition

This retrospective study included 99 clinical studies (36 women and 63 men, mean age = 56.04 ± 12.99 yr, mean weight = 82.03 ± 24.01 kg) consisting of both normal and abnormal patients. There were 99 scans from 99 different patients. Eighty subjects were employed for the training, whereas 19 subjects were used for external validation of the proposed AC model. A mixture of rest and stress studies was used with the number of stress cases (71) more than rest cases (Mehranian *et al.*, 2016). The dataset was randomly split into training and evaluation datasets. Image quality assessment was performed by experienced physicians on non-AC SPECT images. They reported severe diaphragmatic and breast attenuation artefacts in seven subjects as reflected in Table 1 (two reported diaphragmatic attenuation artefacts and one ischemia and myocardial infarction belonged to the test dataset). The study was approved by the ethical committee of Mashhad University of Medical Sciences (Ethic number IR.MUMS.REC.1398.235). The patients underwent electrocardiogram (ECG)-gated acquisition of MPI-SPECT stress studies 45–60 min after intravenous injection of 740–925 MBq activity of ^{99m}Tc-sestamibi. SPECT and CT images were acquired on a Discovery NM/CT 670 (GE Healthcare) dual-head SPECT/CT. CT images were acquired with 120 kVp tube potential, 50 mAs tube current, 5 mm slice thickness, 512 × 512 matrix size, and a voxel size of 0.97 × 0.97 × 5 mm^3. The SPECT data were acquired with a low-energy high-resolution collimator using 30 projections per detector with 25 seconds per projection (the total number of projections was 60 acquired on a dual-head SPECT/CT camera) covering a 180-degree rotation with a zoom factor of 1.3. Owing to the sequential acquisition of SPECT and CT images, which increases the potential of patient movement and misalignment errors, image registration between SPECT and CT images was performed using the Xeleris ^{TM} platform, and noticeable alignment errors were manually corrected. CT-based AC was performed to generate reference SPECT-MPI images. These deep learning models were trained to directly estimate attenuation-corrected SPECT images from uncorrected images without the

use of anatomical images. Scatter correction was applied on the projection data using the dual-energy window and triangular approximation method. In addition to the photopeak window, a lower energy window (92–125 keV) within the Compton spectrum was defined to estimate the magnitude and spatial distribution of scattered photons. The reconstruction of both attenuation- and non-attenuation-corrected SPECT images (matrix size of 64 × 64 × 40 and voxel resolution of 6.79 × 6.79 × 6.79 mm^3) was performed using the ordered subset expectation maximization algorithm with 4 iterations, 10 subsets, and a post-reconstruction Butterworth filter (frequency of 0.4 and power of 10). ECG-gated MPI-SPECT data were acquired using 8 frames per cardiac cycle for R–R interval length using the forward–backward gating method (Hesse *et al.*, 2008; Sarebani *et al.*, 2020). The deep learning-based AC models were trained and evaluated using ungated SPECT images. A mixture of rest and stress myocardial perfusion SPECT images were employed for training and evaluation of the deep learning algorithm. This could be considered as a limitation of this work since AC may be more challenging for rest images owing to the prevalence of extra-cardiac interference.

2.2 Network architecture

In this work, two deep learning models, namely ResNet and UNet, were implemented in TensorFlow using the NiftyNet platform to predict SPECT CT-AC from SPECT non-AC images in the image domain. The NiftyNet framework is an open-source platform, developed upon the TensorFlow module in the Python environment, that provides a high-level deep learning pathway for medical image analysis and processing, including segmentation, classification, and image regression (Gibson *et al.*, 2018).

The ResNet architecture, illustrated in Fig. 1, consists of 20 convolutional layers where all layers, except the last one, are fully connected softmax layer, with 3 × 3 kernels, batch normalization, rectified linear unit (ReLU), and a shortcut connection added to each pair of 3 × 3 filters to enhance the training speed and efficiency (Li *et al.*, 2017). The structure benefits from dilated convolutions (by a factor of 2 for the middle seven layers and a factor of 4 for the last six layers) that support the exponential inflation of the receptive field while preserving the original resolution of the input images.

The UNet architecture, implemented in the NiftyNet platform, is an upgraded version of the traditional convolutional neural network with a 'U' shape and symmetric structure consisting of 23 convolutional layers in 2 major parts (Ronneberger *et al.*, 2015). The first part includes the contracting path (left-hand part in Fig. 2) that follows the general convolutional process, each consisting of two 3 × 3 convolution kernels followed by a ReLU and a 2 × 2 max-pooling operation. At each downsampling step (max-pooling operation), the number of channels increases as the convolution process will increase the depth of the image. The second part is the expansive path (right-hand part in Fig. 2), which consists of upsampling of the feature maps (reducing the number of channels at every step) followed by a
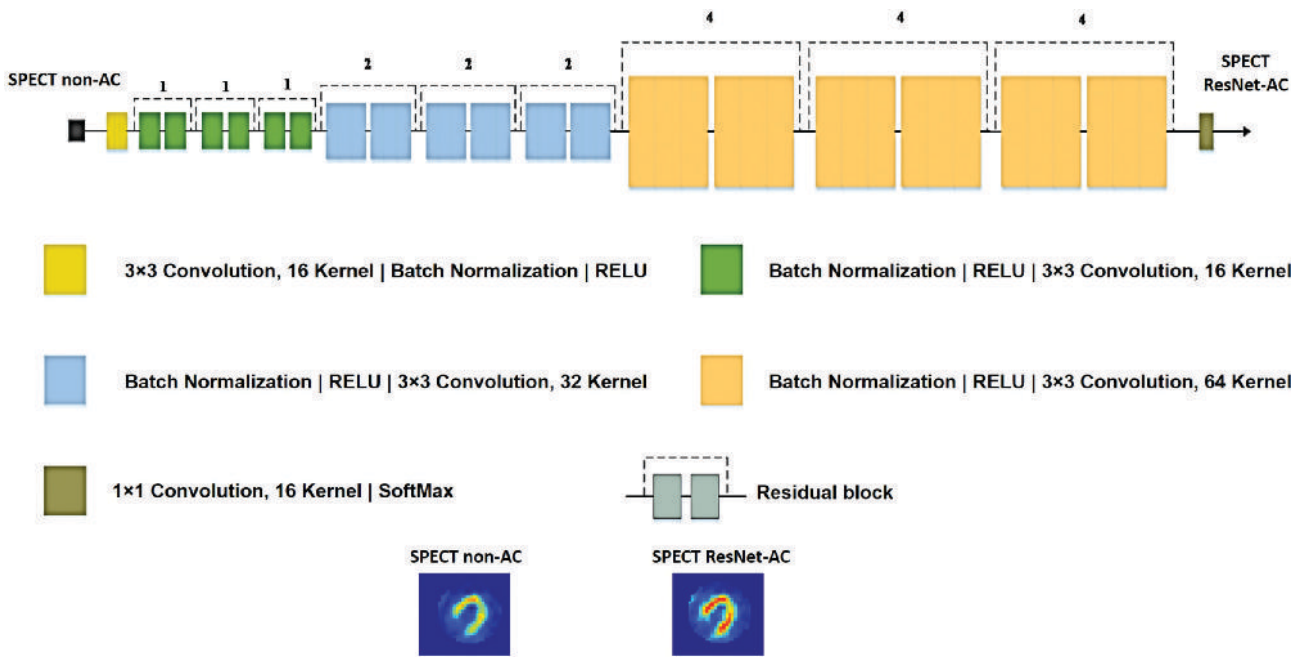
Figure 1: Architecture of the ResNet network implemented in the NiftyNet platform.
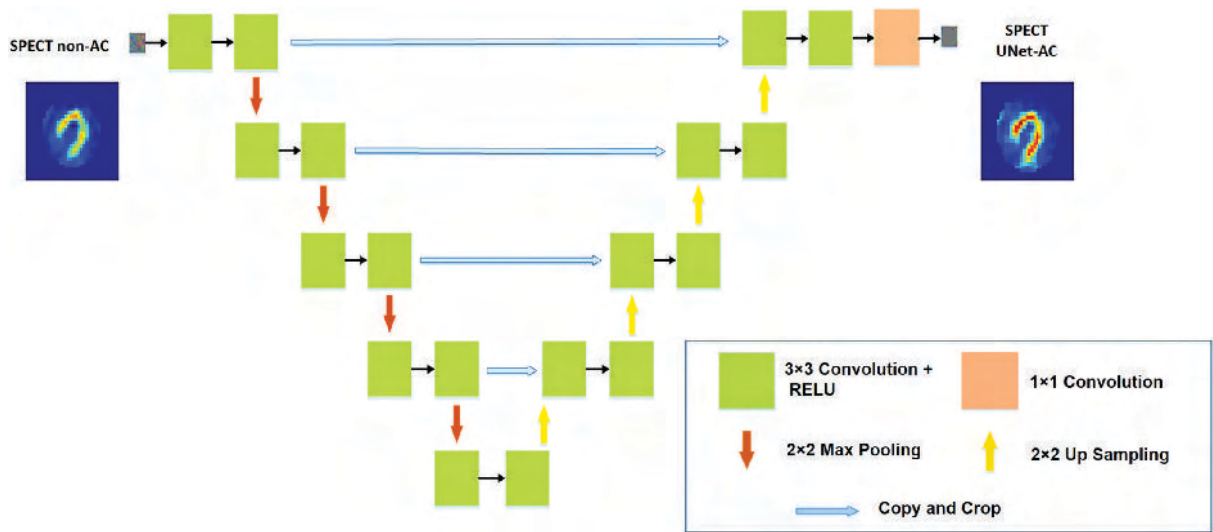

Figure 2: Architecture of the UNet network implemented in the NiftyNet platform.

transposed 2 × 2 convolutional layer (concatenated with the corresponding feature map from the contracting path), two 3 × 3 convolutions, and a ReLU.

2.3 Implementation details

The training of the networks for the prediction of SPECT CT-AC images was performed using 80 randomly selected pairs of SPECT non-AC and SPECT CT-AC images as input and output, respectively. The input images have about 17 slices along the axial direction of the body. Overall, 1360 2D slices were used for training of the models. Nineteen SPECT non-AC images (not used in training) were used as an external validation dataset. 5% of the training dataset was dedicated to model evaluation during the training to verify and avoid the risk of overfitting. SPECT images' pixel values were normalized to 90% of their corresponding cumulative histograms to reduce the variation of intensity range across different patients. Furthermore, irrelevant voxels containing background air were removed through cropping the images into a matrix size of 32 × 32 voxels for UNet and ResNet models' training to reduce the computational burden.

The ResNet model was trained using the following parameters: learning rate = 0.0001, optimizer = Adam, loss function = L2 Loss, weight decay = 0.0001, batch size = 40, and total iterations of 19k. The training for the UNet model was performed using the same loss function, decay, and batch size, but the learning rate was 0.001. The training of the UNet was completed after almost 18k iterations since its training loss reached its plateau. It should
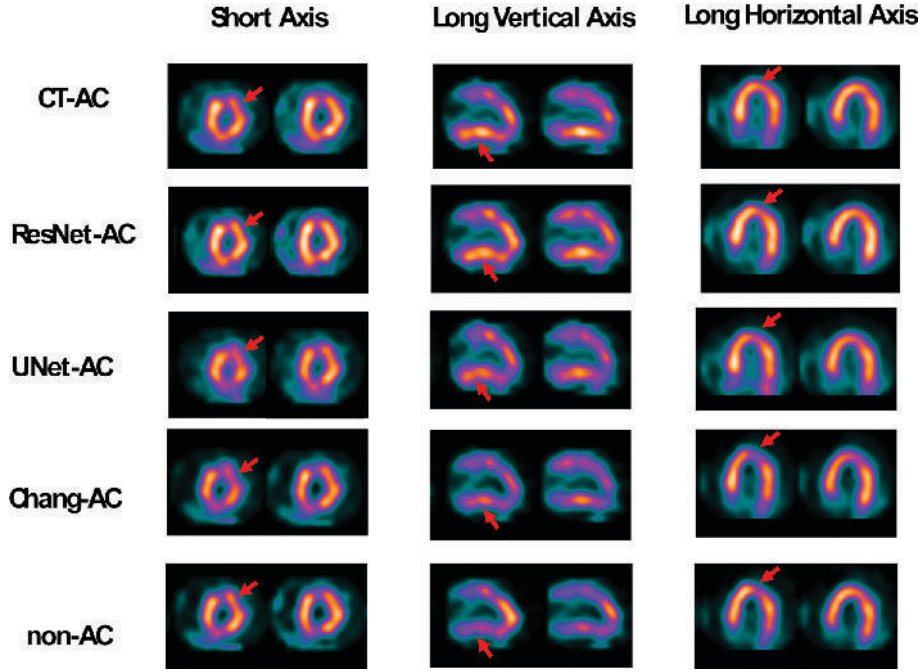
Figure 3: Representative MPI-SPECT images of a patient (30-year-old male, normal in stress phase) showing from top to bottom: SPECT CT-AC images, attenuation-corrected SPECT images generated by the ResNet and UNet models, and attenuation-corrected SPECT images using Chang's technique as well as uncorrected SPECT images.

be noted that the training of these models was performed in 2D mode (using 2D slices). Previous experience with 2D and 3D implementations of AC in the image domain motivated the choice of 2D over 3D implementation (Shiri *et al.*, 2020). The 2D implementation of the deep learning-guided AC model led to overall superior performance and fewer image artefacts (or outliers).

2.4 Evaluation strategy

Quantitative evaluation of the synthetic SPECT images generated by the ResNet and UNet models was performed against the reference SPECT CT-AC images. Calculated Chang's AC technique was also implemented to provide a baseline for comprehensive performance assessment of the deep learning models. This method assumes a mean uniform attenuation coefficient of 0.09 cm^{-1} within the body contour. A lower attenuation coefficient was selected given that the thorax region contains low-density lung tissue bearing low photon attenuation factors (Izadyar *et al.*, 2011). An empirical threshold of 5 (pixel counts) was considered based on the intensity of SPECT images, wherein the body contours of 11 subjects were manually corrected to avoid any gross errors.

The quantitative accuracy of MPI-SPECT AC images was estimated using the following quantitative metrics: voxel-wise mean error (ME; equation 1), mean absolute error (MAE; equation 2), root mean square error (RMSE; equation 3), and relative error (RE%; equation 4) calculated between SPECT CT-AC and SPECT-AC images (generated by the two deep learning models and Chang's method).

$$ME = \frac{1}{N} \sum_{i=1}^{N} dS(i) \tag{1}$$

$$MAE = \frac{1}{N} \sum_{i=1}^{N} |dS(i)| \tag{2}$$

$$RMSE = \sqrt{\frac{1}{N} \sum_{i=1}^{N} (dS(i))^2} \tag{3}$$

$$RE(\%) = \frac{1}{N} \sum_{i=1}^{N} \frac{dS(i)}{S_R(i)} \times 100 \tag{4}$$

Here, N indicates the total number of voxels in the volume of interest, $dS(i) = (S_C(i) - S_R(i))$, $S_R(i)$ is the reference image (SPECT CT-AC), $S_C(i)$ is the attenuation-corrected image using one of the three different methods, and i stands for the voxel index in the SPECT-AC and SPECT CT-AC images. Moreover, the peak signal-to-noise ratio (PSNR) and structural similarity index (SSI) were calculated between the different SPECT-AC images versus the reference SPCET CT-AC images using equations (5) and (6), respectively (Arabi *et al.*, 2020).

$$PSNR = 10 \log \left(\frac{I^2}{MSE} \right) \tag{5}$$

$$SSI = \frac{(2\mu_R\mu_C + K_1)(2\delta_{R,C} + K_2)}{(\mu_R^2 + \mu_C^2 + K_1)(\delta_R^2 + \delta_C^2 + K_2)} \tag{6}$$

In equation (5) (Garcia, 2007), I represents the maximum intensity of either SPECT CT-AC or different SPECT-AC, whereas MSE is the mean square error. In equation (6), μ_R and μ_C indicate the mean value of SPECT CT-AC and SPECT-AC images, respectively. δ_R and δ_C are the variances of SPECT CT-AC and SPECT-AC images, respectively, whereas $\delta_{R,C}$ indicates their covariance. The parameters $K_1 = (k_1 I)^2$ and $K_2 = (k_2 I)^2$ with constants $k_1 = 0.01$ and $k_2 = 0.02$ were introduced to avoid division by very small numbers. Furthermore, the voxel-wise correlation of the tracer uptake between the ResNet, UNet, and Chang's methods versus the reference SPECT CT-AC images was calculated using joint histogram analysis.

The perceptual quality scores and semantic scores are useful metrics for the evaluation of the resulting SPECT images
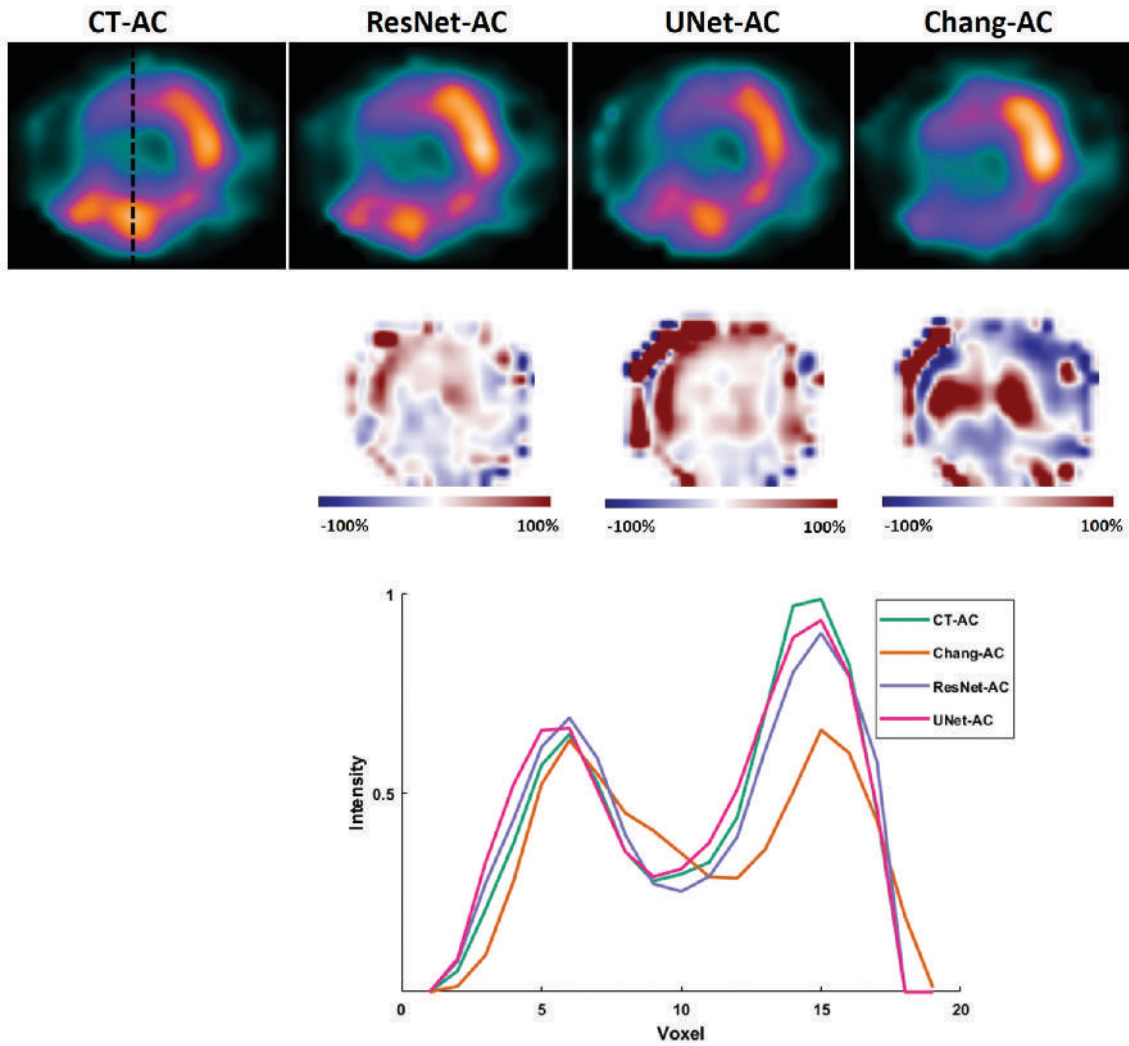
Figure 4: Representative short-axis views of SPECT CT-AC, SPECT ResNet-AC, SPECT UNet-AC, and SPECT Chang-AC of a patient (30-year-old male, normal in stress phase) along with relative bias (%) maps with respect to the reference SPECT CT-AC images. Line profiles drawn through the myocardium are also shown, and the dashed line on the CT-AC image shows the location of the drawn profile.

Table 2: Statistical analysis of image quality metrics calculated on attenuation-corrected MPI-SPECT images reconstructed using the different methods with respect to the reference SPECT CT-AC images.

Methods	ME (counts)	MAE (counts)	RMSE (counts)	RE (%)	SSI	PSNR
ResNet-AC	-6.99 ± 16.72	20.24 ± 17.63	42.33 ± 32.41	-0.34 ± 15.03	0.99 ± 0.04	28.15 ± 4.17
UNet-AC	-4.41 ± 11.85	13.65 ± 11.23	36.10 ± 26.1	0.42 ± 15.88	0.98 ± 0.05	29.44 ± 3.45
Chang-AC	25.52 ± 33.98	80.27 ± 47.56	83.06 ± 27.98	11.74 ± 31.67	0.93 ± 0.09	22.06 ± 2.50

(Seitzer *et al.*, 2018). However, the parameters employed in the present study are standard/conventional metrics utilized in similar works. Hence, we opted to use these parameters to be comparable with previous studies.

Clinical assessment was performed through calculating quantitative parameters extracted from Cedars-Sinai Medical Center software, Quantitative Perfusion SPECT (QPS). These quantitative parameters include Defect, Extent, Summed Stress Percent (SS%), Summed Stress Score (SSS), Total Perfusion Deficit (TPD%), Volume, Area, Shape Eccentricity (ECC), and Shape Index (SI).

3. Results

Figure 3 provides views along the short and long axes for a representative clinical study, comparing SPECT ResNet-AC, SPECT UNet-AC, and SPECT Chang-AC along with the corresponding SPECT CT-AC. It can be seen that the deep learning-based predicted images bear image quality comparable to reference SPECT CT-AC, while noticeable differences were observed on Chang-AC images.

Representative long vertical axis views of SPECT CT-AC, SPECT ResNet-AC, SPECT UNet-AC, and SPECT Chang-AC images
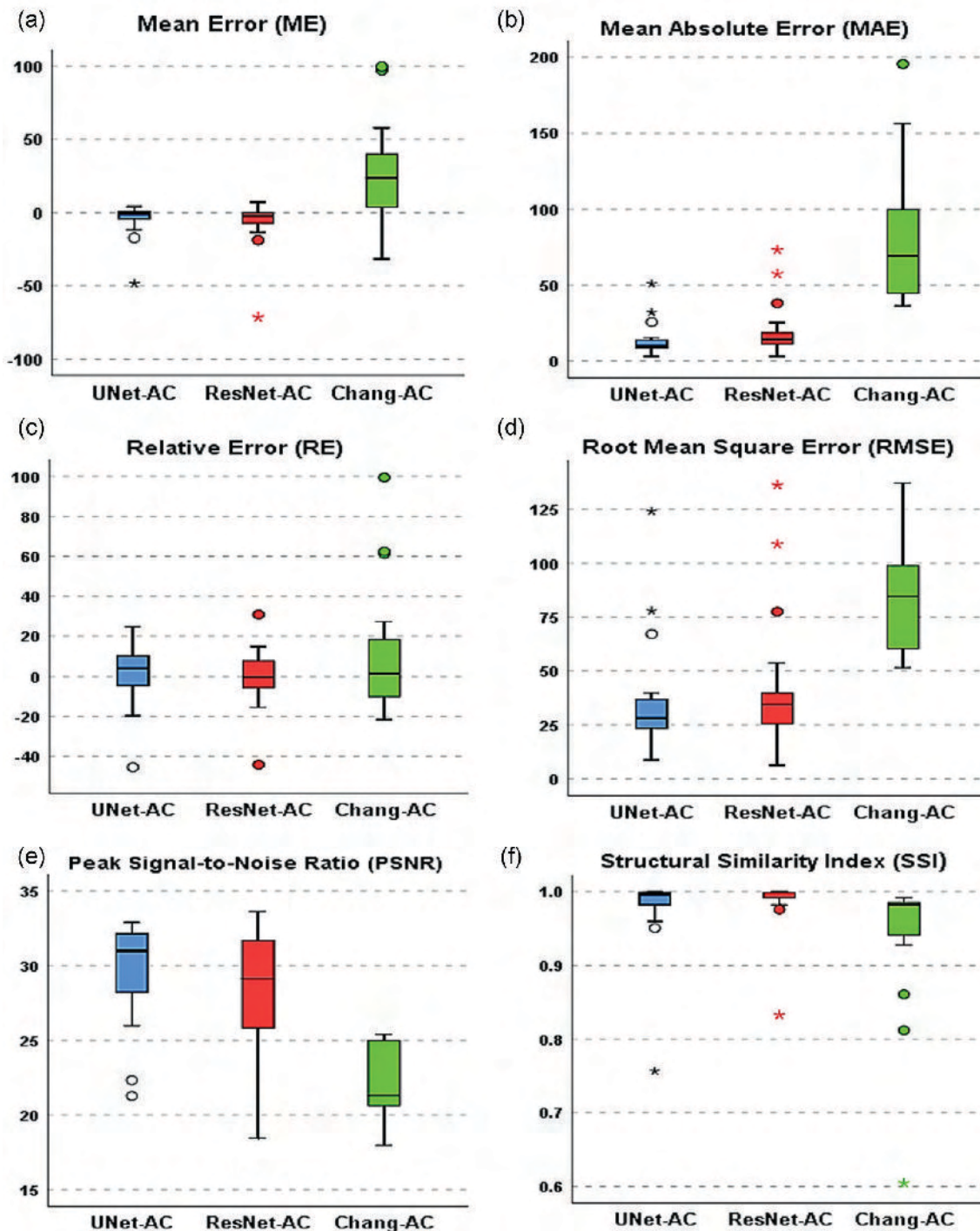
Figure 5: Comparison of (a) ME, (b) MAEs, (c) RE%, (d) RMSEs, (e) PSNR, and (f) SSI, calculated in attenuation-corrected SPECT images using the different methods versus the reference SPECT CT-AC.

along with the relative bias maps (%) with respect to reference SPECT CT-AC images are shown in Fig. 4. SPECT ResNet-AC and SPECT UNet-AC revealed good agreement in terms of signal recovery and underlying uptake patterns, while SPECT Chang-AC images exhibited a remarkable underestimation/overestimation of the activity concentration in some regions. This is well depicted on the line profile drawn through the myocardium on

the SPECT CT-AC, SPECT ResNet-AC, SPECT UNet-AC, and SPECT Chang-AC images (Fig. 4).

Table 2 summarizes the results of quantitative metrics (mean ± SD), including ME, MAE, RMSE, RE, SSI, and PSNR, calculated on attenuation-corrected SPECT-MPI for the different methods across the 19 patients of the external validation dataset. SPECT UNet-AC revealed the smallest voxel-wise ME
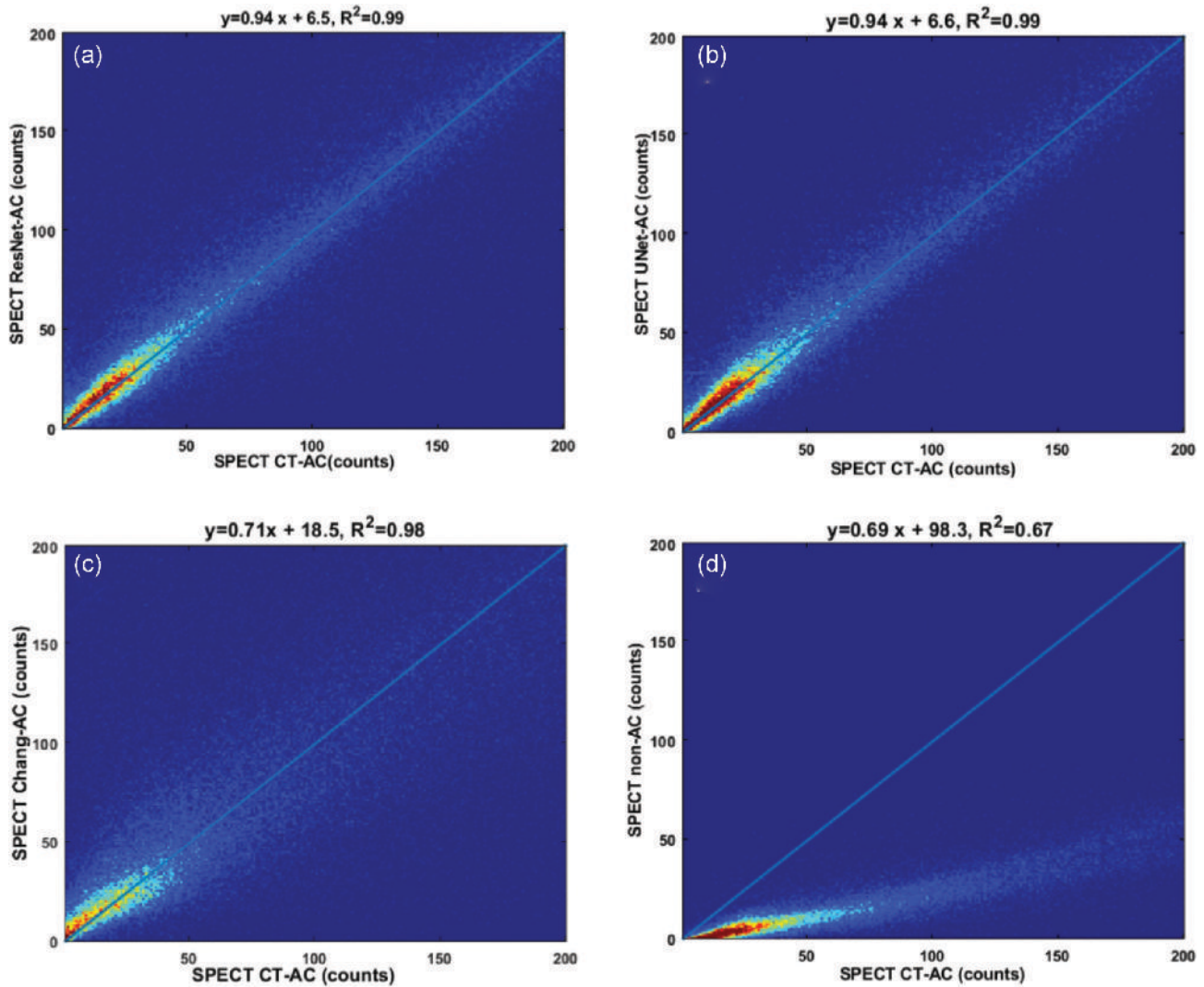
Figure 6: Voxel-wise joint correlation histogram analysis of attenuation-corrected SPECT images using the different methods versus reference SPECT CT-AC images: (a) ResNet, (b) UNet, (c) Chang's methods, and (d) joint correlation histogram analysis of SPECT non-AC versus reference SPECT CT-AC images.
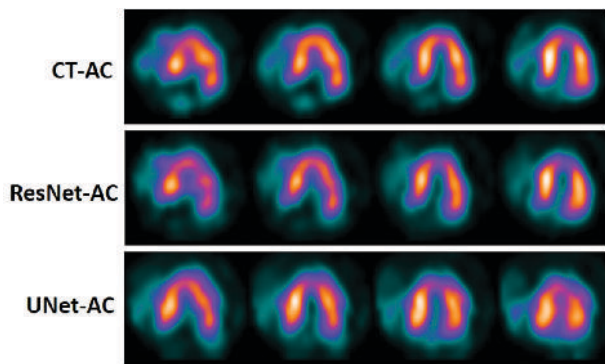

Figure 7: Outlier report: Axial views of SPECT-MPI (58-year-old male, normal in stress phase) showing from left to right: SPECT CT-AC, SPECT ResNetAC, and SPECT UNet-AC images where the UNet-AC model resulted in gross errors.

(-4.41 ± 11.85), MAE (13.65 ± 11.23), and RMSE (42.33 ± 32.41) among the three evaluated models.

Figure 5 presents box plots of ME, MAE, RMSE, RE (%), RMSE, and SSI metrics calculated for the different attenuation-corrected MPI-SPECT images. The joint histogram analysis illustrating the voxel-wise correlation between the reference SPECT CT-AC images and SPECT images corrected for attenuation using the different techniques demonstrates that SPECT images corrected for attenuation using UNet and ResNet models are highly correlated ($R^2 = 0.99$) with reference CT-based AC SPECT images (Fig. 6).

In addition to the assessment of quantification errors, the resulting AC SPECT images were visually examined to determine the number and severity of outliers (or gross errors) indicating the uncertainty of the model. In this regard, the outliers were reported separately to assess the uncertainty of the proposed methods (Schlemper et al., 2018). Figure 7 illustrates a representative case study where the UNet model exhibited gross errors (outlier report). This patient had noticeably lower ^{99m}Tc-sestamibi uptake in the heart compared to other patients in the dataset.

Table 3 summarizes the statistical analysis results obtained from the quantitative assessment of MPI-SPECT images across the 19 patients of the external validation dataset. Regarding the TPD (%) index, SPECT images reconstructed using ResNet (12.78 ± 9.22) and UNet (12.57 ± 8.93) models exhibited good

Table 3: Descriptive statistics of quantitative perfusion analysis of MPI-SPECT images for the different attenuation-corrected images using the Cedars-Sinai-QPS software.

Methods		SSS	SS (%)	TPD (%)	Defect (cm^2)	Extend (%)	Volume (ml)	Area (cm^2)	SI	ECC
CT-AC	Mean ± SD	9.94 ± 6.31	14.31 ± 9.04	12.84 ± 8.63	21.57 ± 17.24	15.84 ± 11.07	89.89 ± 41.52	130.63 ± 32.66	0.59 ± 0.09	0.82 ± 0.05
	Min	0	0	2	2	1	26	75	0.43	0.72
	Max	25	37	35	56	42	185	191	0.75	0.91
ResNet-AC	Mean ± SD	9.68 ± 6.12	14.21 ± 9.07	12.78 ± 9.22	20.78 ± 17.52	15.73 ± 11.36	87.57 ± 39.72	127.94 ± 31.82	0.62 ± 0.10	0.81 ± 0.04
	Min	1	1	1	1	1	24	72	0.44	0.75
	Max	25	37	36	56	42	178	183	0.80	0.90
UNet-AC	Mean ± SD	8.89 ± 6.50	13 ± 9.63	12.57 ± 8.93	21.10 ± 19.33	14.89 ± 12.10	92.05 ± 42.05	132.47 ± 32.33	0.60 ± 0.09	0.83 ± 0.03
	Min	3	4	3	2	2	23	70	0.42	0.75
	Max	26	38	34	61	42	191	197	0.80	0.90
Chang-AC	Mean ± SD	12.94 ± 9.15	19.05 ± 13.37	16.68 ± 11.24	24.94 ± 19.70	20.05 ± 14.14	77.00 ± 42.48	115.10 ± 35.61	0.63 ± 0.07	0.80 ± 0.04
	Min	3	4	5	3	4	16	56	0.52	0.73
	Max	34	50	39	59	47	183	185	0. 80	0.88
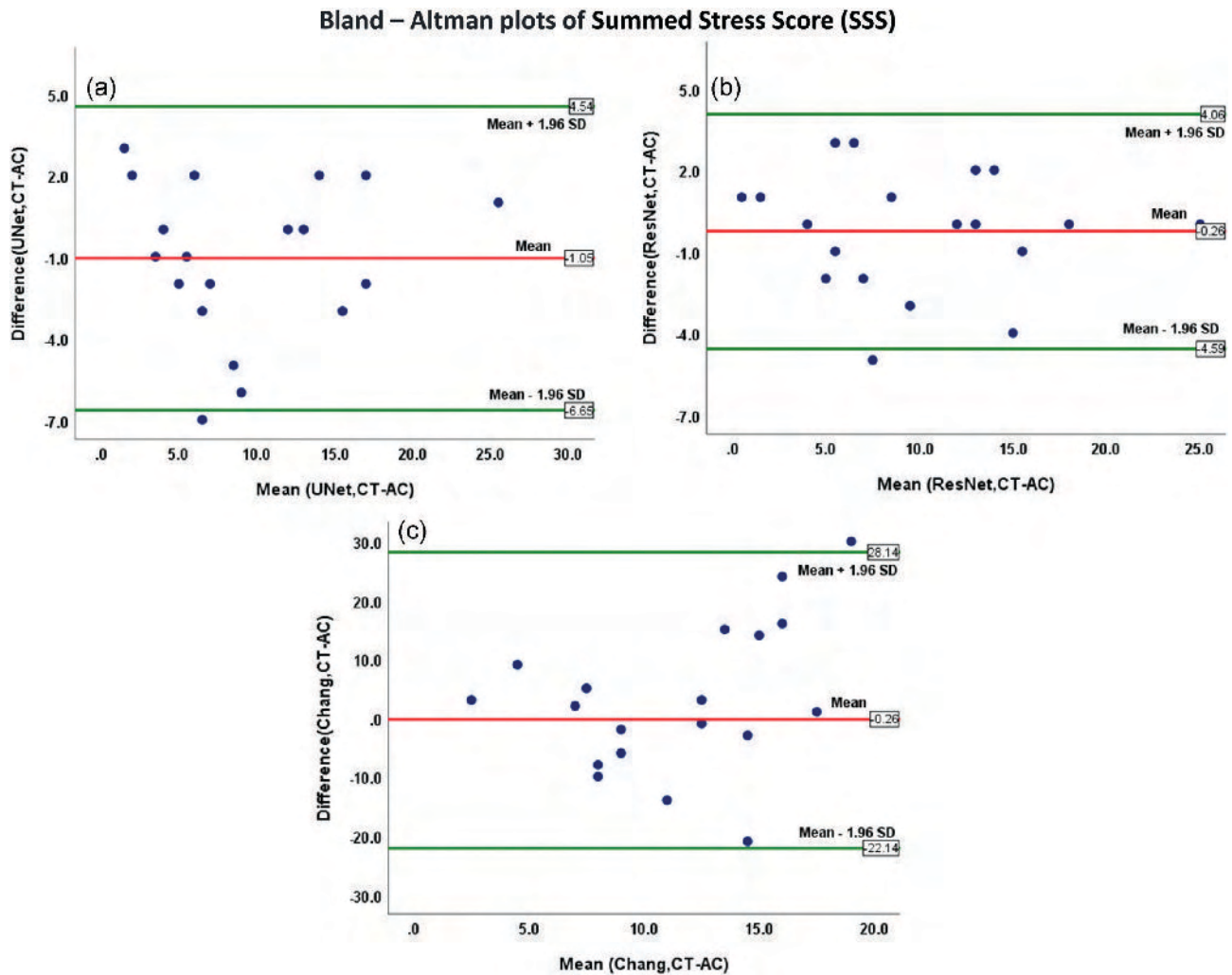
Figure 8: Bland–Altman plots of SSS calculated between (a) UNet and CT-AC methods, (b) ResNet and CT-AC methods, and (c) Chang and CT-AC methods.

agreement with the reference CT-AC images (12.84 ± 8.63). Detailed information about the distribution of TPD (%), SS (%), and SSS indices is shown in the box plots depicted in Supplemental Fig. 2.

The Bland–Altman plots for SSS, PDD, and defect metrics calculated between CT-AC and the different AC methods are presented in Figs 8–10. It was observed that 95% of the data points for the deep learning models lie within ±1.96 SD of the mean difference, while the differences between the metrics calculated

from Chang and CT-AC methods are significantly larger than the two other AC methods.

A Wilcoxon signed-rank test was performed for ResNet and UNet models, wherein statistically significant differences were observed in RMSE and MAE metrics ($Z = -3.743$, $p < 0.02$ for MAE and $Z = -2.857$, $p < 0.005$ for RMSE), demonstrating slightly better performance of the UNet model. The results of Wilcoxon signed-rank test showed that there are no statistically significant differences in SSS and TPD (%) metrics for the ResNet and
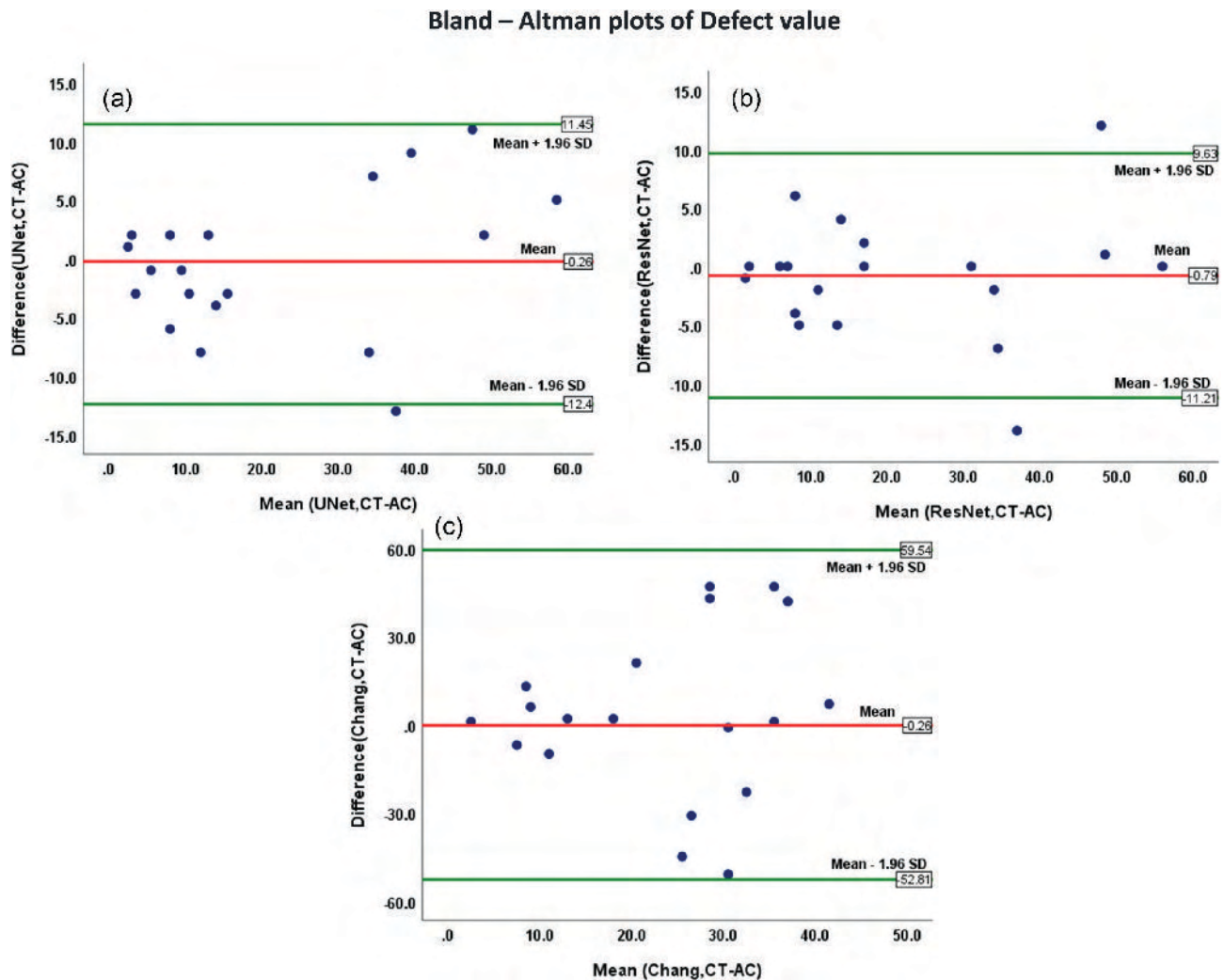
Figure 10: Bland and Altman plots of Defect metric calculated between (a) UNet and CT-AC methods, (b) ResNet and CT-AC methods, and (c) Chang and CT-AC methods.

Unet models [$Z = -1.235$, $p = 0.217$ for SSS and $Z = 0.345$, $p = 0.730$ for TPD (%)].

4. Discussion

In this work, we investigated the possibility of direct AC of ^{99m}Tc-sestamibi SPECT-MPI in the image domain using deep learning-based models. The quantitative results achieved from the analysis of the external dataset consisting of 19 patients demonstrated that the deep learning-based approaches (namely ResNet and UNet) were able to produce attenuation-corrected MPI-SPECT images, featuring an excellent agreement with the reference CT-based attenuation-corrected MPI-SPECT images. Calculated Chang's AC method was also implemented to provide a baseline for insightful performance assessment of the deep learning-based solutions. Though Chang's method was mainly designed for applications in brain imaging and is less applicable in the thorax and pelvis regions owing to the heterogeneity of the attenuating medium, this method enables partial recovery of the signal loss caused by attenuated or scattered photons. As such, this technique would provide relatively improved image quality/contrast (compared to non-AC image) and can be considered as an alternative AC approach on trans-

missionless SPECT cameras or to decrease the radiation dose to patients. The deep learning models outperformed Chang's AC method as demonstrated by the quantitative image-derived metrics.

The deep learning-based AC models developed in this work are capable of modelling/compensating for photon attenuation and associated artefacts, such as mismatch between emission and transmission scans (Shiri et al. 2020, ; Yang et al., 2021b). Since the majority of the training samples are pairs of aligned SPECT images without and with AC, the deep learning networks would accurately model the deficiencies due to photon attenuation and artefacts related to mismatches between emission and transmission scans. However, other artefacts resulting from the acquisition/system or patient motion, which are almost similar on both non-AC and AC SPECT images, would not be corrected by these AC models. To account for such artefacts, dedicated deep models should be developed/trained using simulation or artefact-free datasets (Lim et al., 2019; Arabi & Zaidi, 2020c, 2021; Lyu et al., 2021).

CT-based AC is routinely performed on hybrid SPECT/CT systems in clinical practice, thus enabling quantitative MPI-SPECT imaging taking advantage of accurate, low-noise, patient-specific AC maps. However, this hybrid imaging modality suffers
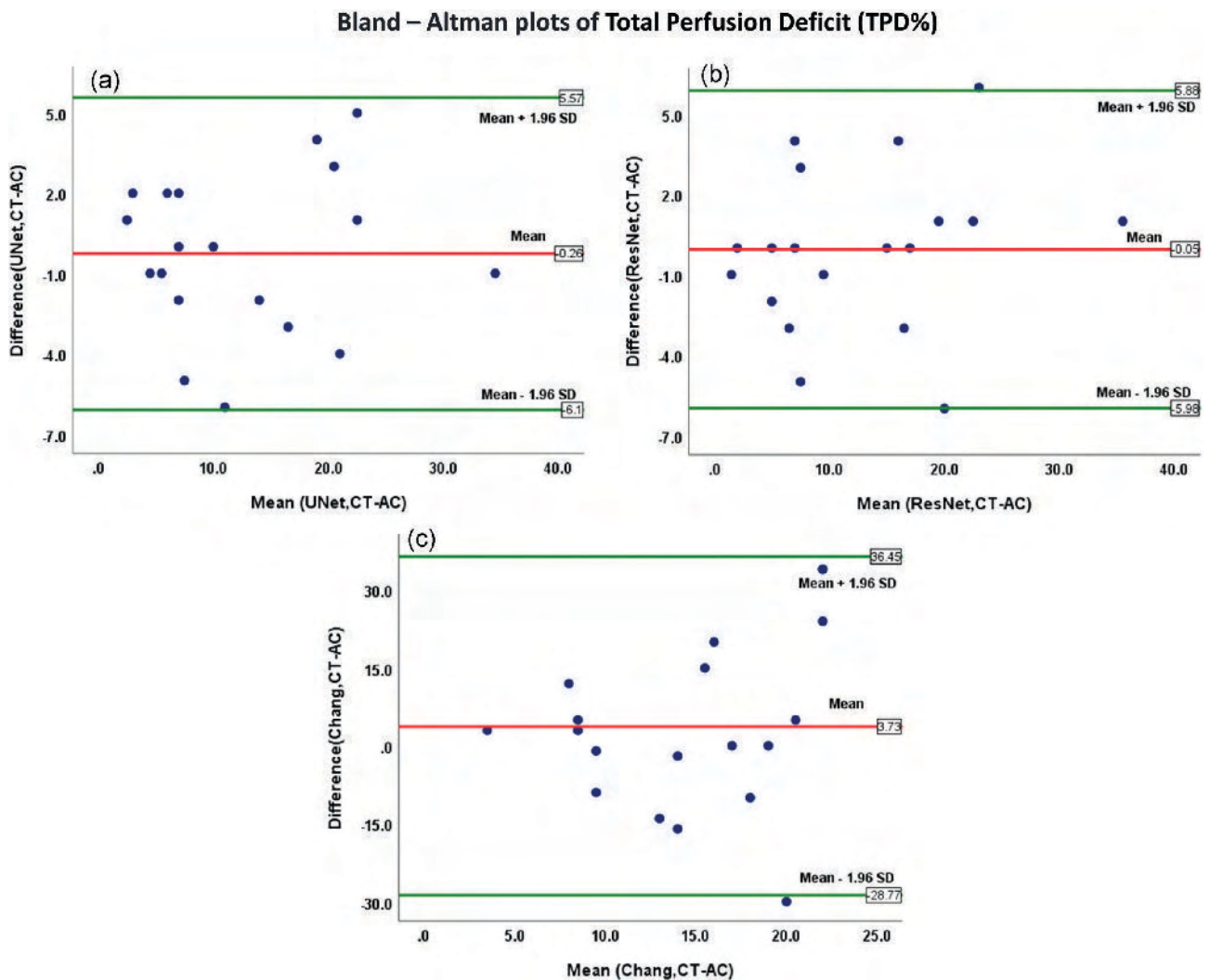
Bland – Altman plots of Total Perfusion Deficit (TPD%)

Figure 9: Bland–Altman plots of TPD% calculated between (a) UNet and CT-AC methods, (b) ResNet and CT-AC methods, and (c) Chang and CT-AC methods.

from a number of limitations, including additional patient radiation exposure and potential misregistration between CT and SPECT images that may cause quantitative uncertainty or image artefacts (Goetze et al., 2007; Dickson, 2019). Deep learning-based AC in the image domain would eliminate the need for transmission scanning or CT-derived AC maps. Deep learning-based AC in the image domain for PET imaging demonstrated a promising capability to account for the misalignment between emission and transmission images owing to respiratory or patient bulk motions (Shiri et al., 2020; Mostafapour et al., 2021b; Zaidi & El Naqa, 2021).

In recent years, deep learning methods have been increasingly applied for AC in PET, reporting promising results for the generation of AC maps from MR images or direct AC of non-attenuation-corrected PET in the image domain (Arabi et al., 2019, 2020; Dong et al., 2020). However, fewer studies have been conducted on the use of deep learning-based AC in SPECT imaging (Marshall et al., 2011; Arabi & Zaidi, 2020a) owing to the smaller availability of SPECT/MR hybrid systems in clinical setting (Hutton et al., 2018). In this regard, Shi et al. (Shi et al., 2020) proposed a novel framework wherein MPI-SPECT images of both photopeak and scatter energy windows, interconnected as a multichannel image, were fed into a generative adversar-

ial network (GAN). Their GAN model used a modified 3D version of a U-net architecture as a generator and a typical CNN architecture as a discriminator. A GAN model enables the estimation of patient-specific AC map from scatter and photopeak images, relying on the existing complementary information between these images. The quantitative analysis of this approach performed on 25 patients revealed a normalized mean absolute error (NMAE) of 3.60 ± 0.85% between synthetic and CT-based attenuation maps, leading to accurate AC in SPECT-MPI (Shi et al., 2020). In a recent study, Nguyen et al. proposed a 3D Unet-GAN network (the 3D GAN network model that uses 3D UNet as the generator), generating attenuation-corrected MPI-SPECT from non-attenuation-corrected SPECT as input (Nguyen et al., 2020). The results of this work showed that their proposed model could generate synthetic SPECT-AC images with SSI = 0.945% and NMAE = 0.034 compared to the reference SPECT CT-AC image.

Torkaman et al. employed a conditional generative adversarial network (cGAN) based on the Pix2Pix model for direct AC of SPECT-MPI. They also extended the proposed model to Wasserstein cGAN to improve the stability of the optimization process. The quantitative evaluation revealed a normalized RMSE (NRMSE) of 0.14 ± 0.08, a PSNR of 36.38 ± 3.74, and an SSI of

0.99 ± 0.00 for the cGAN model (Torkaman *et al.*, 2021). This study lacked detailed clinical evaluation of the proposed method. In another study, Yang *et al.* investigated direct AC in the image space for cardiac stress-only ^{99m}Tc-tetrofosmin SPECT-MPI. They exploited a 3D UNet-based network for the direct generation of attenuation-corrected SPECT images from non-AC ones. Scatter correction was not considered in this study (reference CT-based AC was performed without scatter correction). Voxel-wise and segment-wise analyses were performed to evaluate the generated AC SPECT images versus reference CT-based AC for 100 patients. Their model achieved an NRMSE of 0.15 ± 0.09, a PSNR of 36.2 ± 4.1, and an SSI of 0.99 ± 0.01 in voxel-wise analysis. Segment-wise analyses of the resulting cardiac SPECT images based on the American Heart Association 17 segments in the myocardium revealed reduced attenuation artefacts, though the deep learning AC model resulted in some outliers (Yang *et al.*, 2021a).

The magnitude of errors observed in this work is in good agreement with previous studies, which indicates that deep learning solutions enable one to achieve robust and repeatable synthesis of MPI-SPECT images with clinically tolerable errors. The deep learning models exhibited less than 10% quantification errors for most of the subjects in the test dataset (Table 2), which are commonly considered as clinically tolerable errors (Zaidi, 2006). This observation is supported by the clinical results summarized in Table 3, wherein the two deep learning-based AC approaches exhibited almost similar results compared to CT-based AC. In this light, it was concluded that the deep learning AC methods have the potential to achieve reliable AC in MPI-SPECT imaging. These deep learning AC frameworks could be employed on standalone SPECT-only or SPECT/MR cameras to achieve reliable quantitative imaging. Nevertheless, further studies are required to evaluate the feasibility of this method using larger databases covering different radiotracers, body regions, and acquisition protocols, in the presence of a broad range of defects/diseases.

5. Conclusion

This study investigated the potential of direct AC of ^{99m}Tc-sestamibi MPI-SPECT images in the image domain using deep learning-based algorithms. The clinical and quantitative evaluations revealed that the deep learning AC methods have the potential to achieve reliable AC in MPI-SPECT imaging.

Acknowledgments

Conflict of interest statement

None declared.

References

Akamatsu, M., Yamashita, Y., Akamatsu, G., Tsutsui, Y., Ohya, N., Nakamura, Y., & Sasaki, M. (2014). Influences of reconstruction and attenuation correction in brain SPECT images obtained by the hybrid SPECT/CT device: Evaluation with a 3-dimensional brain phantom. *Asia Oceania Journal of Nuclear Medicine & Biology*, 2(1), 24.

Arabi, H., & Asl, A. R. K. (2010). Feasibility study of a new approach for reducing of partial volume averaging artifact in CT scanner. In *17th Iranian Conference of Biomedical Engineering (ICBME)*(pp. 1–4).

Arabi, H., Rager, O., Alem, A., Varoquaux, A., Becker, M., & Zaidi, H. (2015). Clinical assessment of MR-guided 3-class and 4-class attenuation correction in PET/MR. *Molecular Imaging and Biology*, 17, 264–276.

Arabi, H., & Zaidi, H. (2016). Whole-body bone segmentation from MRI for PET/MRI attenuation correction using shape-based averaging. *Medical Physics*, 43, 5848.

Arabi, H., & Zaidi, H. (2017). Comparison of atlas-based techniques for whole-body bone segmentation. *Medical Image Analysis*, 36, 98–112.

Arabi, H., Dowling, J. A., Burgos, N., Han, X., Greer, P. B., Koutsouvelis, N., & Zaidi, H. (2018). Comparative study of algorithms for synthetic CT generation from MRI: Consequences for MRI-guided radiation planning in the pelvic region. *Medical Physics*, 45, 5218–5233.

Arabi, H., Zeng, G., Zheng, G., & Zaidi, H. (2019). Novel adversarial semantic structure deep learning for MRI-guided attenuation correction in brain PET/MRI. *European Journal of Nuclear Medicine and Molecular Imaging*, 46, 2746–2759.

Arabi, H., & Zaidi, H. (2020a). Applications of artificial intelligence and deep learning in molecular imaging and radiotherapy. *European Journal of Hybrid Imaging*, 4(1), 17.

Arabi, H., & Zaidi, H. (2020b). Deep learning-guided estimation of attenuation correction factors from time-of-flight PET emission data. *Medical Image Analysis*, 64, 101718.

Arabi, H., & Zaidi, H. (2020c). Truncation compensation and metallic dental implant artefact reduction in PET/MRI attenuation correction using deep learning-based object completion. *Physics in Medicine and Biology*, 65, 195002.

Arabi, H., Bortolin, K., Ginovart, N., Garibotto, V., & Zaidi, H. (2020). Deep learning-guided joint attenuation and scatter correction in multitracer neuroimaging studies. *Human Brain Mapping*, 41(13), 3667–3679.

Arabi, H., & Zaidi, H. (2021). Deep learning-based metal artefact reduction in PET/CT imaging. *European Radiology*, 31(8), 6384–6396.

Bahrami, A., Karimian, A., Fatemizadeh, E., Arabi, H., & Zaidi, H. (2020). A new deep convolutional neural network design with efficient learning capability: Application to CT image synthesis from MRI. *Medical Physics*, 47, 5158–5171.

Bahrami, A., Karimian, A., & Arabi, H. (2021). Comparison of different deep learning architectures for synthetic CT generation from MR images. *Physica Medica*, 90, 99–107.

Chang, L.-T. (1978). A method for attenuation correction in radionuclide computed tomography. *IEEE Transactions on Nuclear Science*, 25(1), 638–643.

Chen, Y., Firmin, D., & Yang, G. (2021). Wavelet improved GAN for MRI reconstruction. In *Medical Imaging 2021: Physics of Medical Imaging*(Vol. 11595, pp. 1159513). SPIE.

Cuocolo, A. (2011). Attenuation correction for myocardial perfusion SPECT imaging: Still a controversial issue. *European Journal of Nuclear Medicine and Molecular Imaging*, 38, 1887–1889.

Dickson, J. C. (2019). Quantitative SPECT: A survey of current practice in the UK Nuclear Medicine Community. *Nuclear Medicine Communications*, 40(10), 986–994.

Dong, X., Lei, Y., Wang, T., Higgins, K., Liu, T., Curran, W. J., Mao, H., Nye, J. A., & Yang, X. (2020). Deep learning-based attenuation correction in the absence of structural information for whole-body positron emission tomography imaging. *Physics in Medicine and Biology*, 65(5), 055011.

Esteves, F., Santana, C., Folks, R., Faber, T., Bateman, T., & Garcia, E. (2005). Attenuation-corrected adenosine stress Tc-99m

estamibi myocardial perfusion SPECT normal files: Prospective validation and comparison to exercise stress normal files. *Journal of Nuclear Cardiology*, 4, S124–S125.

Fukushima, Y., & Kumita, S.-i. (2016). Cardiac SPECT/CT imaging: CT attenuation correction and SPECT/CT hybrid imaging. *International Journal of Radiology & Medical Imaging*, 2, 113.

Garcia, E. V. (2007). SPECT attenuation correction: An essential tool to realize nuclear cardiology's manifest destiny. *Journal of Nuclear Cardiology*, 14, 16–24.

Genovesi, D., Giorgetti, A., Gimelli, A., Kusch, A., D'Aragona Tagliavia, I., Casagranda, M., Cannizzaro, G., Giubbini, R., Bertagna, F., Fagioli, G., Rossi, M., Romeo, A., Bertolaccini, P., Bonini, R., & Marzullo, P. (2011). Impact of attenuation correction and gated acquisition in SPECT myocardial perfusion imaging: Results of the multicentre SPAG (SPECT attenuation correction vs gated) study. *European Journal of Nuclear Medicine and Molecular Imaging*, 38, 1890–1898.

Gholamiankhah, F., Mostafapour, S., & Arabi, H. (2021). Deep learning-based synthetic CT generation from MR images: Comparison of generative adversarial and residual neural networks. *arXiv preprint arXiv:2103.01609*,

Gibson, E., Li, W., Sudre, C., Fidon, L., Shakir, D. I., Wang, G., Eaton-Rosen, Z., Gray, R., Doel, T., Hu, Y., Whyntie, T., Nachev, P., Modat, M., Barratt, D. C., Ourselin, S., Cardoso, M. J., & Vercauteren, T. (2018). NiftyNet: A deep-learning platform for medical imaging. *Computer Methods and Programs in Biomedicine*, 158, 113–122.

Goetze, S., Brown, T. L., Lavely, W. C., Zhang, Z., & Bengel, F. M. (2007). Attenuation correction in myocardial perfusion SPECT/CT: Effects of misregistration and value of reregistration. *Journal of Nuclear Medicine*, 48, 1090–1095.

Hachamovitch, R., Berman, D. S., Shaw, L. J., Kiat, H., Cohen, I., Cabico, J. A., Friedman, J., & Diamond, G. A. (1998). Incremental prognostic value of myocardial perfusion single photon emission computed tomography for the prediction of cardiac death: Differential stratification for risk of cardiac death and myocardial infarction. *Circulation*, 97, 535–543.

Hesse, B., Lindhardt, T. B., Acampa, W., Anagnostopoulos, C., Ballinger, J., Bax, J. J., Edenbrandt, L., Flotats, A., Germano, G., Stopar, T. G., Franken, P., Kelion, A., Kjaer, A., Le Guludec, D., Ljungberg, M., Maenhout, A. F., Marcassa, C., Marving, J., McKiddie, F., . . . Underwood, R. (2008). EANM/ESC guidelines for radionuclide imaging of cardiac function. *European Journal of Nuclear Medicine and Molecular Imaging*, 35(4), 851–885.

Hutton, B. F., Occhipinti, M., Kuehne, A., Máthé, D., Kovács, N., Waiczies, H., Erlandsson, K., Salvado, D., Carminati, M., Montagnani, G. L., Short, S. C., Ottobrini, L., van Mullekom, P., Piemonte, C., Bukki, T., Nyitrai, Z., Papp, Z., Nagy, K., & Niendorf, T., . . . INSERT Consortium.(2018). Development of clinical simultaneous SPECT/MRI. *British Journal of Radiology*, 91(1081), 20160690.

Iskander, S., & Iskandrian, A. E. (1998). Risk assessment using single-photon emission computed tomographic technetium-99m sestamibi imaging. *Journal of the American College of Cardiology*, 32(1), 57–62.

Izadyar, S., Saber, S., & Gholamrezanezhad, A. (2011). Assessment of clinical impact in the application of Chang attenuation correction to lung ventilation/perfusion SPECT. *Journal of Nuclear Medicine Technology*, 39(4), 290–294.

W. Li, G. Wang, L. Fidon, S. Ourselin, M. J. Cardoso, & T. Vercauteren , eds, (2017). On the compactness, efficiency, and representation of 3D convolutional networks: Brain parcellation as a pretext task. In *International Conference on Information Processing in Medical Imaging*(pp. 348–360). Springer.

Li, G., Lv, J., Tong, X., Wang, C., & Yang, G. (2021). High-resolution pelvic MRI reconstruction using a generative adversarial network with attention and cyclic loss. *IEEE Access*, 9, 105951–105964.

Lim, H., Chun, I. Y., Fessler, J., & Dewaraja, Y. (2019). Improved low count quantitative SPECT reconstruction with a trained deep learning-based regularizer. *Journal of Nuclear Medicine*, 60, 42.

Lyu, Q., Shan, H., Xie, Y., Kwan, A. C., Otaki, Y., Kuronuma, K., Li, D., & Wang, G. (2021). Cine cardiac MRI motion artifact reduction using a recurrent neural network. *IEEE Transactions on Medical Imaging*, 40(8), 2170–2181.

Marshall, H. R., Stodilka, R. Z., Theberge, J., Sabondjian, E., Legros, A., Deans, L., Sykes, J. M., Thompson, R. T., & Prato, F. S. (2011). A comparison of MR-based attenuation correction in PET versus SPECT. *Physics in Medicine and Biology*, 56, 4613–4629.

Masood, Y., Liu, Y. H., Depuey, G., Taillefer, R., Araujo, L. I., Allen, S., Delbeke, D., Anstett, F., Peretz, A., Zito, M. J., Tsatkin, V., & Wackers, F. J. (2005). Clinical validation of SPECT attenuation correction using X-ray computed tomography-derived attenuation maps: Multicenter clinical trial with angiographic correlation. *Journal of Nuclear Cardiology*, 12, 676–686.

Mehranian, A., Arabi, H., & Zaidi, H. (2016). Quantitative analysis of MRI-guided attenuation correction techniques in time-of-flight brain PET/MRI. *Neuroimage*, 130, 123–133.

Mehranian, A., & Zaidi, H. (2015). Joint estimation of activity and attenuation in whole-body TOF PET/MRI using constrained Gaussian mixture models. *IEEE Transactions on Medical Imaging*, 34, 1808–1821.

Mehranian, A., Arabi, H., & Zaidi, H. (2016). Vision 20/20: Magnetic resonance imaging-guided attenuation correction in PET/MRI: Challenges, solutions, and opportunities. *Medical Physics*, 43, 1130–1155.

Mostafapour, S., Arabi, H., Gholamian Khah, F., Razavi-Ratki, S. K., & Parach, A. A. (2021a). Tc-99m (methylene diphosphonate) SPECT quantitative imaging: Impact of attenuation map generation from SPECT-non-attenuation corrected and MR images on diagnosis of metastatic bone, *International Journal of Radiation Research*, 19(2), 299–308.

Mostafapour, S., Gholamian Khah, F., Dadgar, H., Arabi, H., & Zaidi, H. (2021b). Feasibility of deep learning-guided attenuation and scatter correction of whole-body 68Ga-PSMA PET studies in the image domain. *Clinical Nuclear Medicine*, 46(8), 609–615.

T. T. Nguyen, T. N. Chi, M. D. Hoang, H. N. Thai, & T. N. Duc , eds, (2020). 3D Unet generative adversarial network for attenuation correction of SPECT images. In *4th International Conference on Recent Advances in Signal Processing, Telecommunications & Computing (SigTelCom)*(pp. 93–97).

Raza, H., Jadoon, L. K., Mushtaq, S., Jabeen, A., Maqbool, M., Ul Ain, M., Ahmed, B., & Ali Memon, M. (2016). Comparison of non-attenuation corrected and attenuation corrected myocardial perfusion SPECT. *Egyptian Journal of Radiology and Nuclear Medicine*, 47, 783–792.

O. Ronneberger, P. Fischer, & T. Brox , eds, (2015). U-net: Convolutional networks for biomedical image segmentation. In *International Conference on Medical Image Computing and Computer Assisted Intervention*(pp. 234–241). Springer.

Russell, R. R. , III, & Zaret, B. L. (2006). Nuclear cardiology: Present and future. *Current Problems in Cardiology*, 31(9), 557–629.

Sajedi, S., Zeraatkar, N., Moji, V., Farahani, M. H., Sarkar, S., Arabi, H., Teymoorian, B., Ghafarian, P., Rahmim, A., & Reza Ay, M. (2014). Design and development of a high-resolution animal

SPECT scanner dedicated for rat and mouse imaging. *Nuclear Instruments and Methods in Physics Research Section A: Accelerators, Spectrometers, Detectors and Associated Equipment*, 741, 169–176.

Saleki, L., Ghafarian, P., Bitarafan-Rajabi, A., Yaghoobi, N., Fallahi, B., & Ay, M. R. (2019). The influence of misregistration between CT and SPECT images on the accuracy of CT-based attenuation correction of cardiac SPECT/CT imaging: Phantom and clinical studies. *Iranian Journal of Nuclear Medicine*, 27, 63–72.

Sarebani, M., Shiran, M. B., Bitarafan-Rajabi, A., Rastgou, F., Haghighi, Z. O., & Ardakani, A. A. (2020). The impact of frame numbers on cardiac ECG-gated SPECT images with interpolated extra frames using echocardiography. *Medical Journal of the Islamic Republic of Iran*, 34, 57.

J. Schlemper, G. Yang, P. Ferreira, A. Scott, L.-A. McGill, Z. Khalique, M. Gorodezky, M. Roehl, J. Keegan, D. Pennell, D. Firmin, & D. Rueckert , eds, (2018). Stochastic deep compressive sensing for the reconstruction of diffusion tensor cardiac MRI. In *International Conference on Medical Image Computing and Computer-Assisted Intervention*(pp. 295–303). Springer.

M. Seitzer, G. Yang, J. Schlemper, O. Oktay, T. Würfl, V. Christlein, T. Wong, R. Mohiaddin, D. Firmin, J. Keegan, D. Rueckert, & A. Maier , eds, (2018). Adversarial and perceptual refinement for compressed sensing MRI reconstruction. In *International Conference on Medical Image Computing and Computer Assisted Intervention*(pp. 232–240). Springer.

Shi, L., Onofrey, J. A., Liu, H., Liu, Y. H., & Liu, C. (2020). Deep learning-based attenuation map generation for myocardial perfusion SPECT. *European Journal of Nuclear Medicine and Molecular Imaging*, 47, 2383–2395.

Shiri, I., Arabi, H., Geramifar, P., Hajianfar, G., Ghafarian, P., Rahmim, A., Ay, M. R., & Zaidi, H. (2020). Deep-JASC: Joint attenuation and scatter correction in whole-body (18)F-FDG PET using a deep residual network. *European Journal of Nuclear Medicine and Molecular Imaging*, 47(11), 2533–2548.

Singh, B., Bateman, T. M., Case, J. A., & Heller, G. (2007). Attenuation artifact, attenuation correction, and the future of myocardial perfusion SPECT. *Journal of Nuclear Cardiology*, 14, 153–164.

Takavar, A., Eftekhari, M., Beiki, D., Saghari, M., Mostaghim, N., & Sohrabi, M. (2003). Qualitative evaluation of Chang method of attenuation correction on heart SPECT by using custom made heart phantom. *Iranian Journal of Nuclear Medicine*, 20, 13–17.

Tankyevych, O., Tixier, F., Antonorsi, N., Filali Razzouki, A., Mondon, R., Pinto-Leite, T., Visvikis, D., Hatt, M., & Cheze Le Rest, C. (2021). Can alternative PET reconstruction schemes improve the prognostic value of radiomic features in non-small cell lung cancer? *Methods*, 188, 73–83.

Torkaman, M., Yang, J., Shi, L., Wang, R., Miller, E. J., Sinusas, A. J., Liu, C., Gullberg, G. T., & Seo, Y. (2021). Direct image-based attenuation correction using conditional generative adversarial network for SPECT myocardial perfusion imaging. In *Medical Imaging 2021: Biomedical Applications in Molecular, Structural, and Functional Imaging*, (Vol. 11600, pp. 116000U). SPIE.

Yang, J., Shi, L., Wang, R., Miller, E. J., Sinusas, A. J., Liu, C., Gullberg, G. T., & Seo, Y. (2021a). Direct attenuation correction using deep learning for cardiac SPECT: A feasibility study. *Journal of Nuclear Medicine*, 62(11), 1645–1652.

Yang, J., Sohn, J. H., Behr, S. C., Gullberg, G. T., & Seo, Y. (2021b). CT-less direct correction of attenuation and scatter in the image space using deep learning for whole-body FDG PET: Potential benefits and pitfalls. *Radiology: Artificial Intelligence*, 3(2), e200137.

Yuan, Z., Jiang, M., Wang, Y., Wei, B., Li, Y., Wang, P., Menpes-Smith, W., Niu, Z., & Yang, G. (2020). SARA-GAN: Self-attention and relative average discriminator-based generative adversarial networks for fast compressed sensing MRI reconstruction. *Frontiers in Neuroinformatics*, 14, 611666.

H. Zaidi , ed., (2006). Quantitative analysis in nuclear medicine imaging. In *Biosciences*. Springer.

Zaidi, H., & El Naqa, I. (2021). Quantitative molecular positron emission tomography imaging using advanced deep learning techniques. *Annual Review of Biomedical Engineering*, 23, 249–276.

Zaidi, H., & Hasegawa, B. (2003). Determination of the attenuation map in emission tomography. *Journal of Nuclear Medicine*, 44, 291–315.

Zeraatkar, N., Sajedi, S., Farahani, M. H., Arabi, H., Sarkar, S., Ghafarian, P., Rahmim, A., & Ay, M. R. (2014). Resolution-recovery-embedded image reconstruction for a high-resolution animal SPECT system. *Physica Medica*, 30, 774–781.